European Journal of Remote Sensing

ISSN: (Print) (Online) Journal homepage: www.tandfonline.com/journals/tejr20

Wind speed retrieval from the Gaofen-3 synthetic aperture radar for VV- and HH-polarization using a re-tuned algorithm

Weizeng Shao, Ferdinando Nunziata, Youguang Zhang, Valeria Corcione & Maurizio Migliaccio

To cite this article: Weizeng Shao, Ferdinando Nunziata, Youguang Zhang, Valeria Corcione & Maurizio Migliaccio (2021) Wind speed retrieval from the Gaofen-3 synthetic aperture radar for VV- and HH-polarization using a re-tuned algorithm, European Journal of Remote Sensing, 54:1, 318-337, DOI: 10.1080/22797254.2021.1924082

To link to this article: https://doi.org/10.1080/22797254.2021.1924082

Published online: 23 May 2021.

EUROPEAN JOURNAL OF REMOTE SENSING
2021, VOL. 54, NO. 1, 318–337
https://doi.org/10.1080/22797254.2021.1924082

Wind speed retrieval from the Gaofen-3 synthetic aperture radar for VV- and HH-polarization using a re-tuned algorithm

Weizeng Shao [a,b], Ferdinando Nunziata [c], Youguang Zhang [b], Valeria Corcione [c] and Maurizio Migliaccio [c]

[a]College of Marine Sciences, Shanghai Ocean University, Shanghai, China; [b]National Satellite Ocean Application Service, Ministry of Natural Resources, Beijing, 100081, China; [c]Dipartimento Di Ingegneria, Università Degli Studi Di Napoli Parthenope, Napoli, Italy

ABSTRACT

In this study, a re-tuned algorithm based on the geophysical model function (GMF) C-SARMOD2 is proposed to retrieve wind speed from Synthetic Aperture Radar (SAR) imagery collected by the Chinese C-band Gaofen-3 (GF-3) SAR. More than 10,000 Vertical-Vertical (VV) and Horizontal-Horizontal (HH) polarization GF-3 images acquired in quad-polarization stripmap (QPS) and wave (WV) modes have been collected during the last three years, in which wind patterns are observed over open seas with incidence angles ranging from 18° to 52°. These images, collocated with wind vectors from the European Centre for Medium-Range Weather Forecast (ECMWF) reanalysis at 0.125° resolution, are used to re-tune the C-SARMOD2 algorithm to specialize it for the GF-3 SAR (CSARMOD-GF). In particular, the CSARMOD-GF performs differently from the C-SARMOD2 at low-to-moderate incidence angles smaller than about 34°. Comparisons with wind speed data from the Advanced Scatterometer (ASCAT), Chinese Haiyang-2B (HY-2B) and buoys from the National Data Buoy Center (NDBC) show that the root-mean-square error (RMSE) of the retrieved wind speed is approximately 1.8 m/s. Additionally, the CSARMOD-GF algorithm outperforms three state-of-the-art methods – C-SARMOD, C-SARMOD2, and CMOD7 – that, when applied to GF-3 SAR imagery, generating a RMSE of approximately 2.0–2.4 m/s.

ARTICLE HISTORY
Received 2 October 2020
Revised 1 April 2021
Accepted 27 April 2021

Introduction

Wind above the sea surface plays a key role in the atmospheric-marine layer, which governs the exchange of energy and heat across the ocean-air boundary. Additionally, wind plays a critical role in marine meteorology and ocean dynamics research (e.g., sea surface wave and current studies). Furthermore, the extreme winds that characterize hurricanes and typhoons produce some of the most destructive natural disasters on earth and thus require monitoring.

Within this context, microwave satellite remote sensing is a key tool for monitoring wind speed. In the last decade, scatterometers (Hasager et al., 2015; Vogelzang et al., 2011) including the Quick Scatterometer (QuikSCAT), National Aeronautics and Space Administration (NASA)-scatterometer (NSCAT), Advanced Scatterometer (ASCAT), and Chinese Haiyang-2A (HY-2) have been widely used for global monitoring of winds. Scatterometers are particularly useful because their swath width exceeds 500 km and their horizontal resolution can be as fine as 12.5 km. Hence, they are a key tool for researching large-scale interactions between the ocean and atmosphere. However, scatterometer measurements also have limitations, especially in coastal waters. Because scatterometer operational wind products deviate from reality 20 km off the coast, small-scale features produced by coastal dynamics are undetectable (Remmers et al., 2019). Thus, scatterometer wind products are not useful for oceanography research focused on nearshore processes.

It is well known that Synthetic Aperture Radar (SAR) is one of the most efficient instruments for observing the sea surface at high spatial resolution over large areas. For example, the C-band Chinese Gaofen-3 (GF-3) SAR (5.43 GHz) has 8-m/25-m nominal resolution spacing and 30-km/40-km nominal swath coverage for quad-polarization stripmap-I/II (QPS-I/II) mode (Shao et al., 2019a) and a 10-m nominal resolution spacing and 50-km nominal swath coverage for GF-3 SAR in wave (WV) mode (Shao et al., 2019b; Zhu et al., 2018). In the literature, SAR-measured normalized radar cross-sections (NRCS) in the Vertical-Vertical (VV) and Horizontal-Horizontal (HH)-polarized channels, are directly related to the wind vector 10 m above the sea surface (Koch & Feser, 2006; Masuko et al., 1986).

Since Seasat-SAR launched in 1978, the methodology for SAR wind retrieval has been continuously improved (Chapron et al., 2001) by defining

CONTACT Weizeng Shao swz19@tsinghua.org.cn

geophysical model functions (GMF), which are empirical functions to retrieve wind speed from SAR imagery by using a prior information about wind direction and radar incidence angle (Zhou et al., 2017). The C-band GMFs, originally developed for the scatterometer, are tuned with specific C-band SAR data, such as CMOD4 (Stoffelen & Anderson, 1997), CMOD-IFR2 (Komarov et al., 2011; Quilfen et al., 1998), and CMOD5 (Hersbach, 2010; Hersbach et al., 2007). Tuning C-band GMFs with SAR data has also been successfully implemented for ERS-1/2 (Fetterer et al., 1998), ENVISAT-ASAR (Choisnard et al., 2007; Yang et al., 2011a), RADARSAT-1/2 (Komarov et al., 2011; Yang et al., 2011b), SENTINEL-1A/1B (La et al., 2018; Monaldo et al., 2016), and GF-3 SAR (Ren et al., 2017; Shao et al., 2017; Wang et al., 2018; T. Zhang et al., 2019). The newest versions of the CMOD family are CMOD7 (Stoffelen et al., 2017), which is stored as a look-up table, and C-SARMOD2 (Lu et al., 2018). However, since these GMFs are tuned without using GF-3 SAR data, they result in a root-mean-square error (RMSE) of approximately 2 m/s when applied to GF-3 imagery (Li et al., 2018). The coefficient of the C-SARMOD2 algorithm depends on the NRCS, the incidence angle, the wind speed at 10 m, and the wind direction above the sea surface. The goal of this work was to improve the wind speed retrieval from specific GF-3 SAR images by re-tuning the advanced algorithm to compensate for the slight difference of GF-3 SAR from other C-band SAR sensors, for example, SENTINEL-1 and RADARSAT-2 at 5.40 GHz. In addition, as mentioned in Li et al. (2018), the radiometric calibration constants used for converting intensity of GF-3 image into NRCS are not well applicable at some incidence angles, Specifically, utilizing existing calibration constants leads to about a large deviation with the simulations based on CMOD5.N, yielding a greater than 2 dB root-mean-square error (RMSE) of NRCS. One probable cause is the indeterminacy of range pattern, signal transmission attenuation and antenna gain on the sea surface in the imaging process. This aspect also necessitates the development of a GMF for this satellite.

Although most GMFs are defined for the VV channels, HH-polarized GMFs are employed in a few studies (Komarov et al., 2013; Lu et al., 2018). Additionally, a polarization ratio (PR) model (Li et al., 2018; Shao et al., 2014; Vachon & Dobson, 2000; B. Zhang et al., 2011) is commonly employed when applying VV-polarization GMFs to the HH channel. Finally, alternative methods to GMF have been also developed to retrieve wind speed from SAR imagery. In particular, Corcione et al. (2018) relates the azimuthal cut-off wavelength λ_c to the wind speed and tunes a λ_c-based wind retrieval algorithm for X- and C-band SAR. However, this method only works for a fully developed sea state (Grieco et al., 2016).

The backscattered signal of the SAR is slightly different from that of scatterometers; for example, they operate at different C-band frequencies. Most existing GMFs are developed for scatterometer measurements and the various functions of GMFs are empirically designed. Moreover, the PR models have to be re-tuned for each specific frequency, e.g., C-band (B. Zhang et al., 2011) and X-band (Shao et al., 2014), although PR models have similar formulations. In this study, we propose a SAR wind retrieval algorithm based on the C-SARMOD2 formulation using the GF-3 SAR measurements to re-tune the C-SARMOD2 coefficients. More than 10,000 open-sea GF-3 SAR images, acquired in QPS-I/II and WV modes and showing a clear wind-related roughness pattern, are employed to tune the CSARMOD-GMFs for the GF-3 cases at VV- and HH-polarization hereafter the CSARMOD-GF. Collocated winds provided by the European Centre for Medium-Range Weather Forecasts (ECMWF) analysis data at 0.125° resolution, measurements from the Advanced Scatterometer (ASCAT), and buoy observations from the National Data Buoy Center (NDBC) of the National Oceanic and Atmospheric Administration (NOAA) are used to verify the applicability of the proposed GMF and to compare the performance of CSARMOD-GF against other state-of the-art GMFs.

The remainder of this work is organized as follows. The collocated dataset is briefly described in Section 2, including the VV- and HH-polarization GF-3 SAR images and wind data from ECMWF, ASCAT, and NOAA buoys. The methodology for the development of the wind retrieval algorithm is presented in Section 3. The retrieval results and comparisons with results from several existing algorithms are given in Section 4. The paper is summarized and conclusions are presented in Section 5.

Dataset

The GF-3 SAR images were collected during the period from 2016 to 2019, and the product level of the images is stored as Level-1A (L-1A), contain both VV-polarized and HH-polarized channels images. Using an authorized account, these images were accessed from a shared platform provided by the National Satellite Ocean Application Service (NSOAS), which allows public investigators to use GF-3 SAR data for scientific research. More than 10,000 VV- and HH-polarization GF-3

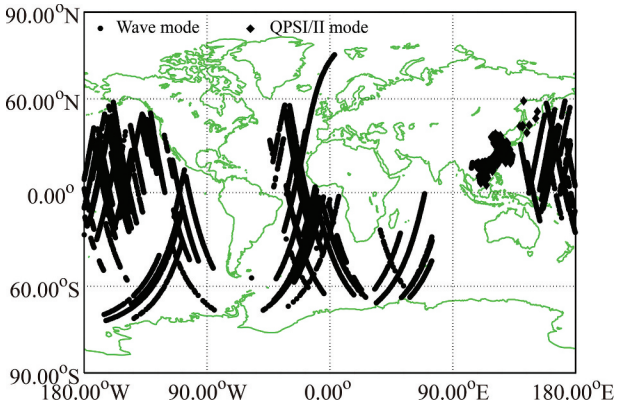

Figure 1. Geographical locations of the Gaofen-3 SAR images for this study. Circles and diamonds represent the footprints of images acquired in wave mode and quad-polarization strip-I (QPS-I) mode, respectively.

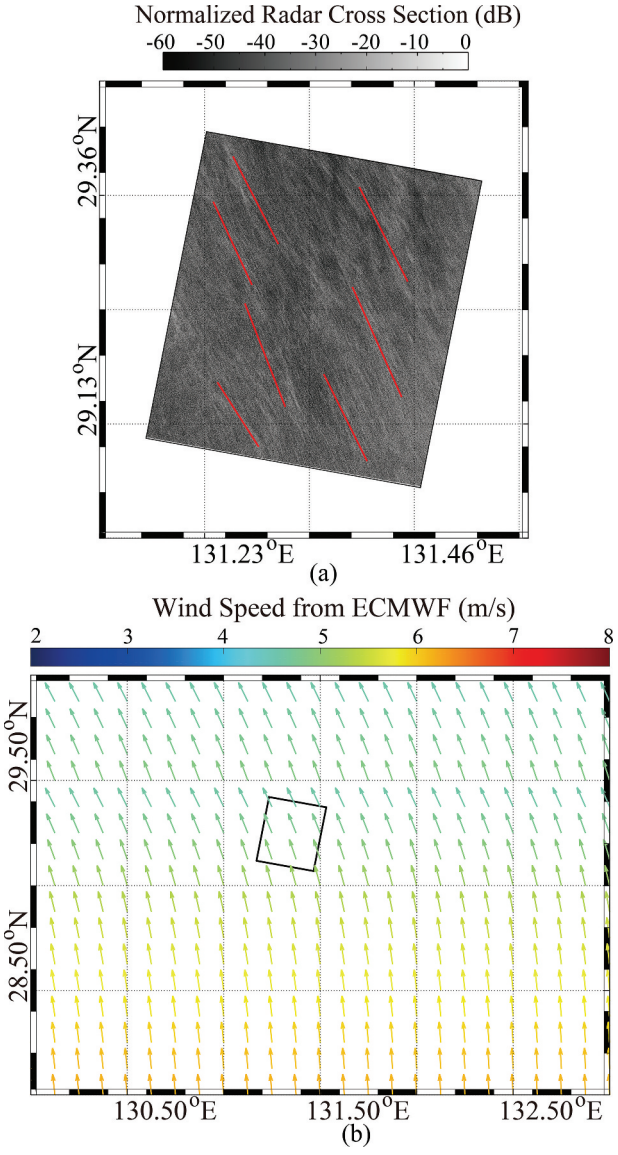

Figure 2. Example of (a) a GF-3 SAR image obtained at 21:14 UTC 29 June 2017, with (b) the corresponding European Centre for Medium-Range Weather Forecast (ECMWF) wind map from 0 UTC 30 June 2017. ECMWF data collocated with the SAR image are indicated by a black box.

images acquired in QPS-I/II and WV modes were collected during the last three years. Figure 1 shows the footprints of available GF-3 images for this study. For calculating the NRCS from VV-

and HH-polarization GF-3 SAR intensity images, the digital number (*DN*) is converted into NRCS following Sheng et al. (2018):

$$\sigma^0 = \mathrm{DN}^2\left(\frac{\mathrm{M}}{32767}\right)^2 - \mathrm{N[dB]}, \quad (1)$$

Previous research confirms that SAR images contain structured line-like patterns parallel to the local wind direction on spatial scales of 800–3000 m (Alpers & Brummer, 1994; Gerling, 1986). These patterns are called "wind streaks" (Koch & Feser, 2006; Zhao et al., 2016), although this type of SAR-derived wind direction has a 180° ambiguity. In this study, wind analysis data from the ECMWF ERA-Interim are obtained at 0.125° resolution to remove the 180° ambiguity of wind direction derived from SAR imagery. Because the GF-3 SAR images have a swath coverage of about 100 km, the sub-scenes extracted from SAR that cover the ECMWF grids data are selected. Next, ECMWF winds are temporally interpolated to one-hour intervals using a cubic spline interpolation (Wang et al., 2018); the time difference between each SAR image and its corresponding interpolated ECMWF data is less than 30 min. Then, the procedure for wind direction retrieval proposed in Shao et al. (2014) is adopted. The technique requires three steps: (1) empirically obtain the prior directions following the visible wind streaks in a man-machine interactive manner, as indicated by the red lines in Figure 2a; (2) search the distance between ECMWF-interpolated wind directions and the locations of prior direction is minimum, thereby taking the matched ECMWF-interpolated wind directions as the "true" wind directions to remove the ambiguity; and (3) apply an Cressman interpolation method: take the available SAR-derived wind directions as inputs and the difference distance between sub-scenes with known wind directions and each sub-scene assumed to be constraint variable with an weight of 5 km. Noted that ECMWF-interpolated wind directions are directly used if there are no visible winds streaks (~20% of total images). The derived wind directions are used for tuning the algorithms. Moreover, the inhomogeneous GF-3 SAR sub-scenes are excluded where the ratios of image variance and squared image mean values were smaller than 1.05 (Li et al., 2011).

In the collocated dataset, wind speeds reach values up to 20 m/s and the incidence angle ranges from 18° to 52°, however, the limitation of collocated dataset is relative smaller amount at moderate winds (> 10 m/s). The spatial difference between ECMWF and GF-3 is less than 1.5 km and the time difference is less than 0.5 h. An example of a calibrated GF-3 SAR image in VV-polarization and its corresponding ECMWF wind field, which is spatially averaged over a 13.9-km grid, is shown in Figure 2. This image with an incidence angle ranging from 35° to 38° was acquired at 21:14 UTC 29 June 2017 and sub-scenes were extracted, which each have a 3 km × 3 km spatial coverage to remove the distortion induced from other atmospheric and marine phenomena. The 3 km × 3 km coverage contains 128 × 128 pixels with a 25-m pixel size for QPS mode and 256 × 256 pixels with a 10-m pixel size for WV mode. In total, we acquired more than 10,000 points for tuning the algorithm, in which the ECWMF wind speeds are collocated with the wind directions, the incidence angles and the NRCSs from GF-3 images. It was found that the ECMWF wind speeds are generally biased low relative to those from the National Centers for Environmental Prediction (NCEP), by approximately −0.4 m/s. The ECMWF also underestimates the wind speed (Stopa & Cheung, 2014) compared with satellite and buoy observations and this magnitude of underestimation (about 10%) could impact the development of the CSARMOD-GF.

ASCAT, which is a new-generation all-weather European active microwave scatterometer onboard Metop-A/B, routinely provides wind speed and direction that can be used to make a preliminary evaluation of SAR-derived wind speeds from Sentinel-1A images (Monaldo et al., 2016). ASCAT operational products, including winds at 10 m above the sea surface, have been available at 0.25° resolution from February 2007 through the present. ASCAT winds were generated using the CMOD5.N algorithm (Hersbach, 2010) until September 2018 and have used the new CMOD7 algorithm (Stoffelen et al., 2017) since then. Although the spatial difference between buoy and GF-3 is less than 1.5 km and the time difference is less than 1.5 h, the consistency of ASCAT and SAR-derived wind directions, meaning that both of them are located at the same quadrant, are ensured so as to determine no severe variation of winds, as illustrated in Figure 3. Moreover, more than 200 GF-3 SAR images in 2020 collocated with the measured winds from Haiyang-2B (HY-2B) scaterometer with a spatial resolution of 25 km are additionally collected in China Seas. Figure 3 exhibits the HY-measured winds map at 08:10 UTC on 30 October 2020, in which rectangles correspond to a few collocated GF-3 SAR images. Noted that the time difference between GF-3 SAR and HY-2B is less than 0.5 h.

Besides, 73 GF-3 SAR images were available for this study covering the locations of NDBC buoys in U.S. coastal waters, indicating the spatial difference between buoy and GF-3 is less than

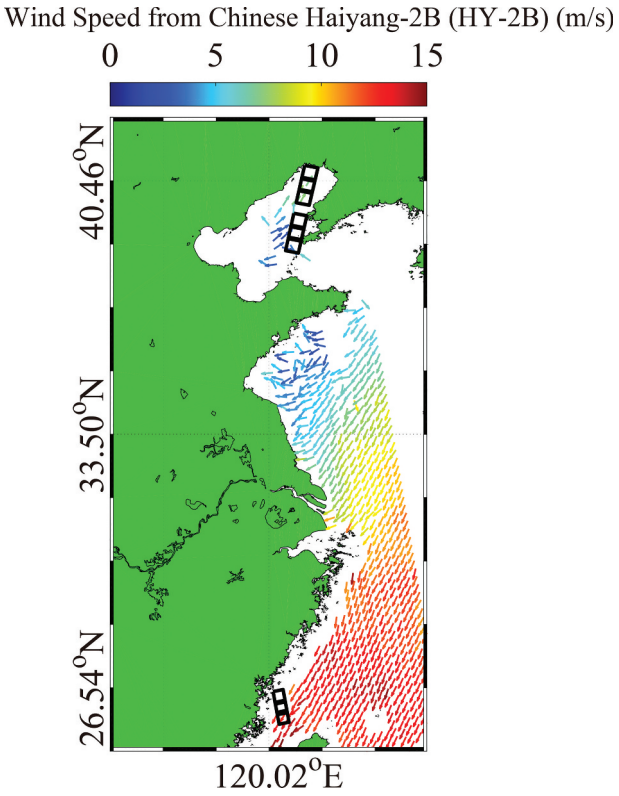

Figure 3. The Chinese Haiyang-2B (HY-2B) wind map at 08:10 UTC on 30 October 2020, in which rectangles correspond to a few collocated GF-3 SAR images.

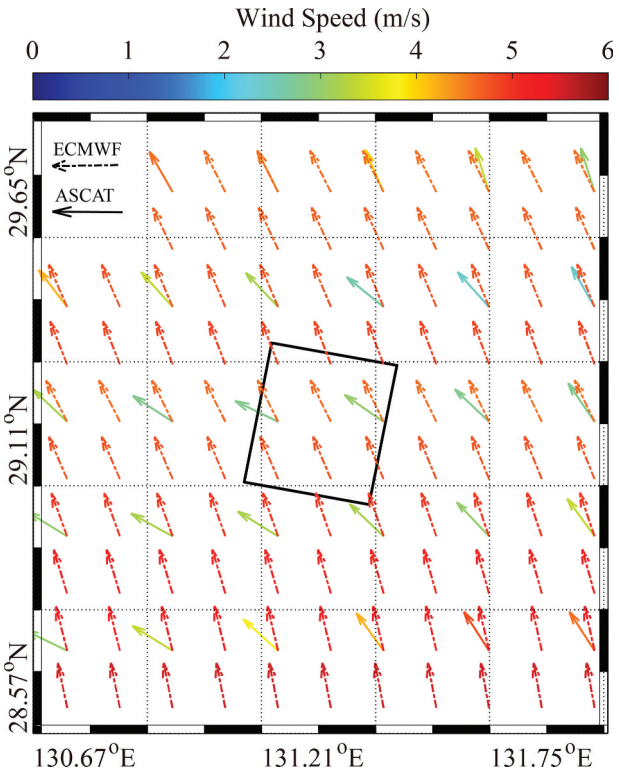

Figure 4. ASCAT wind map at 20:48 UTC 29 June 2017 overlaid by the ECMWF vectors at 18:00 UTC. The black rectangle represents the spatial coverage of the GF-3 SAR image with an incidence angle ranging from 35° to 38° acquired at 21:14 UTC 29 June 2017.

1.5 km and the time difference is less than 0.5 h. Hence, the sub-scenes of each GF-3 SAR image covering the geographic locations of ASCAT products and/or NDBC buoys were selected to compare with the corresponding ASCAT data and the measurements from NDBC buoys. As an example, an ASCAT wind map at 20:48 UTC 29 June 2017 overlaying the ECMWF wind vector

field at 18:00 UTC is shown in Figure 4, in which the black rectangle represents the spatial coverage of the SAR image. In this case, the ASCAT-measured wind speed represented by the solid lines is about 3 m/s within the SAR image, which is similar to the wind speed from ECMWF (about 4 m/s) represented by the dashed lines. Figure 5a and b present histograms for the ECMWF winds up to 20 m/s and ASCAT wind speed estimates for a 1 m/s bin used in this study, showing the mean bias is −0.39 m/s. Similarly, Figure 5c shows the histogram for the incidence angles of tuning dataset ranged from 20° to 50° for a 5° bin.

CSARMOD-GF

In this section, the CSARMOD-GF algorithm is presented and discussed. Figure 6 shows the comparison between VV-polarization NRCS from the GF-3 SAR and simulated NRCS based on the GMF-CMOD5 (Hersbach et al., 2007) using the collocated ECMWF winds, indicating that the RMSE is about 2.8 dB, with 0.67 COR (R^2). This behavior was also found when

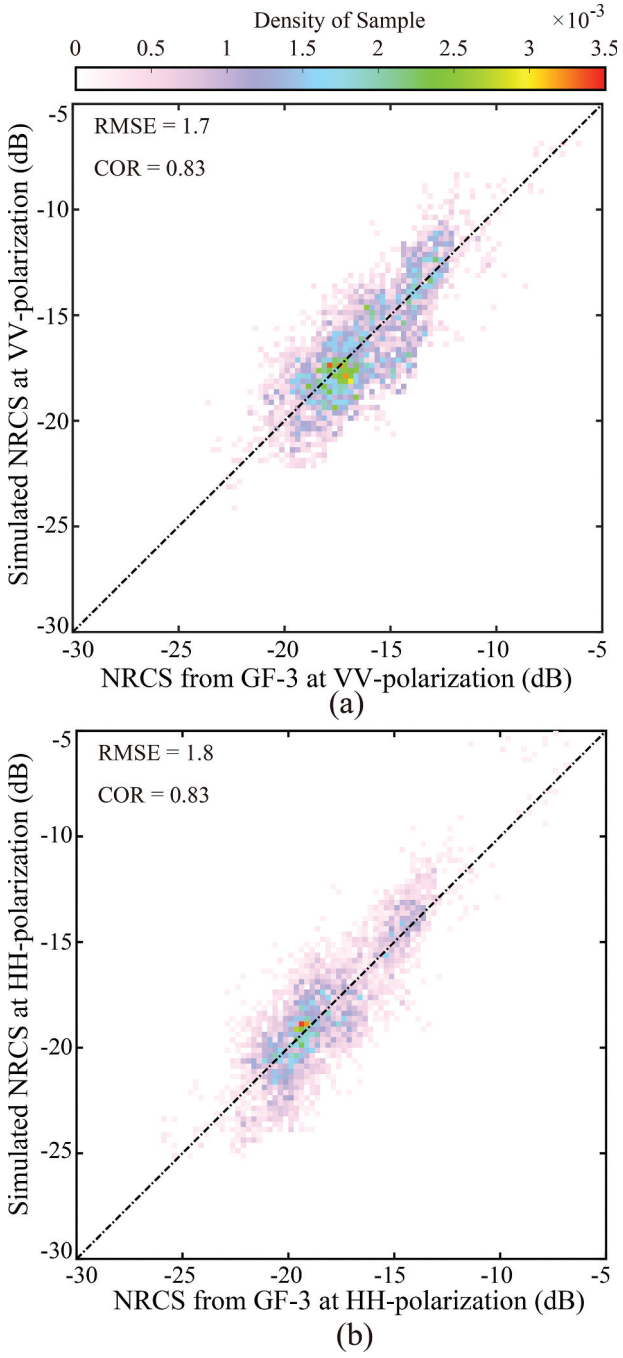

Figure 5. (a) Histogram of collected ECMWF winds; (b) histogram of collected ASCAT winds; (c) the histogram for the incidence angles of tuning dataset.

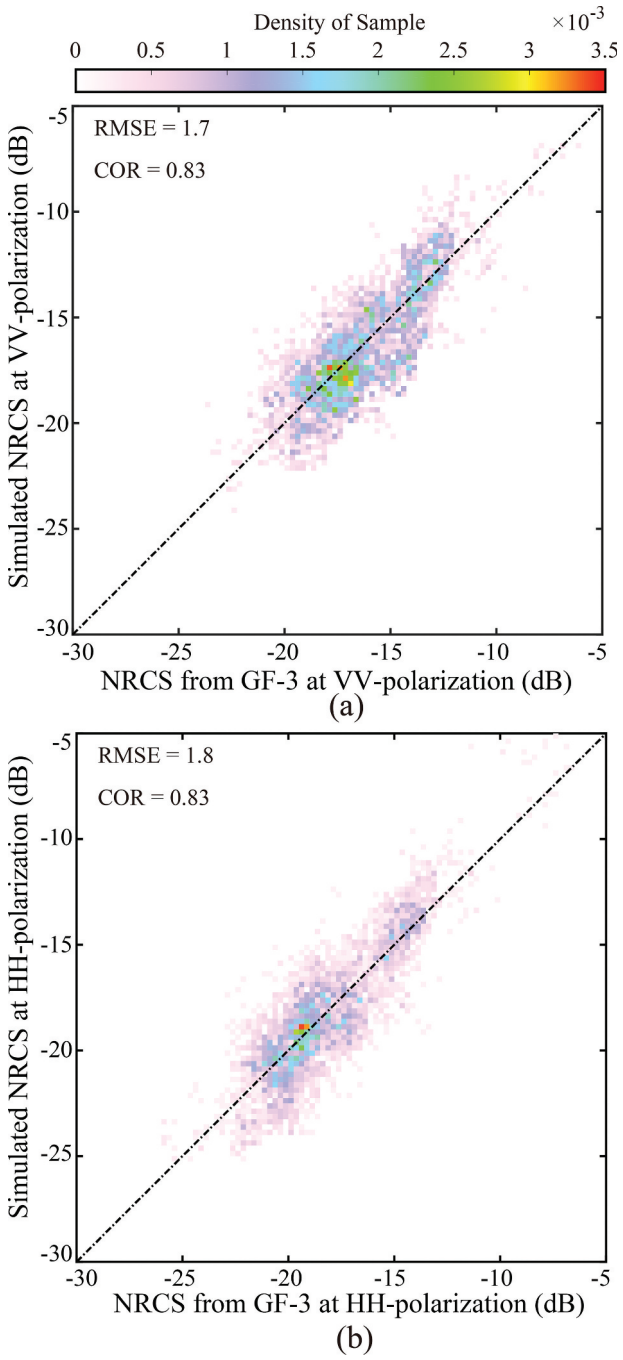

Figure 6. Scatter plot comparing the VV-polarization NRCS with the simulated NRCS based on the GMF-CMOD5 using collocated ECMWF winds.

comparing the simulated NRCS from CMOD5.N and GF-3 SAR NRCS (Li et al., 2018), prompting the effort to improve the wind retrieval for GF-3 SAR using a specific GMF.

The GF-3 VV- and HH-polarization NRCS are compared with ECMWF wind speeds in the density plot of Figure 7a and b. For both polarizations, there is a near-linear relationship between ECMWF wind speed and NRCS. The red lines, which represent mean NRCS values for each 2 m/s ECMWF wind speed bin at a fix incidence angle of about 35° as well the incidence angles of 25° and 45°±2, show that the NRCS using the VV-polarization channel is larger than the NRCS using the HH-polarization channel, which is consistent with the variations of PR ($=\sigma^{HH}/\sigma^{VV}$) on incidence angles, as stated in Figure 7c. Therefore, based on C-SARMOD2 formulation, the GMF is re-tuned to calculate wind speed from VV-polarization and HH-polarization GF-3 SAR images. It is worth noting that the sea surface will generate fewer Bragg waves at low wind speeds U_{10}

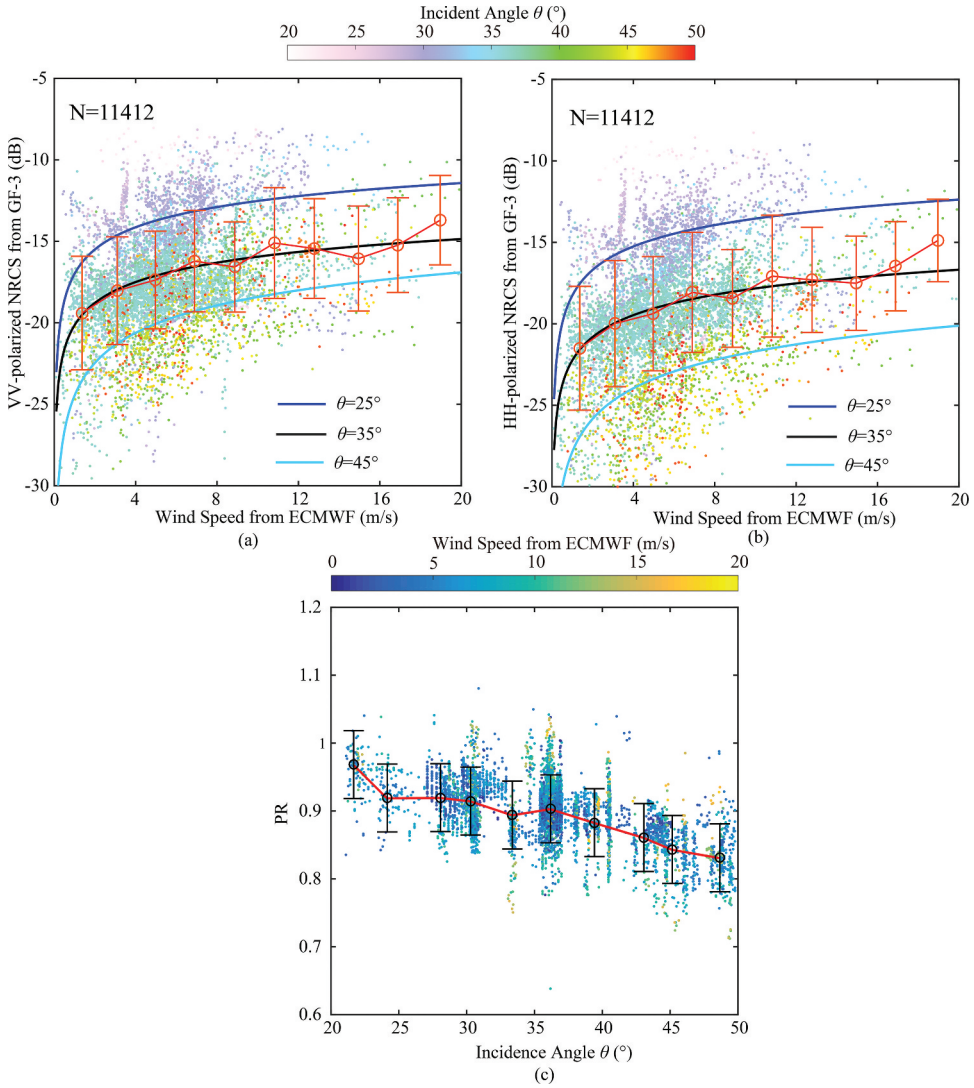

Figure 7. Scatter plot comparing the (a) VV-, and (b) HH-polarization NRCS with ECMWF wind speed at various incidence angles θ. The red line represents the mean NRCS value for each 2 m/s ECMWF wind speed bin at a fix incidence angle about 35°, while error bars represent the standard deviation of NRCS within each ECMWF bin. The black line represents the fitted results.

smaller than 2 m/s, resulting in weak sea surface roughness. Because this kind of Bragg scattering is non-linear at low wind speeds, the slopes of the re-tuned algorithm change significantly at low wind speeds (Figure 7). The detailed CSARMOD-GF algorithm (C-SARMOD2) is presented in the appendix of the investigation by Lu et al. (2018); hence, we do not repeat it here. In Figure 8, NRCS values calculated using the CSARMOD-GF are contrasted with the (a) VV-, and (b) HH-polarization GF-3 NRCS measured over a tuning data set. The COR (R^2) between the calculated and observed values is 0.83 and the RMSE is approximately 1.8 dB, which represent significant improvements compared with the analysis results in Figure 6. For this data set, wind speed values up to 20 m/s are evaluated. We did not consider larger wind speed values, because the SAR backscattered signal encounters saturation at VV- and HH-polarization channels at higher wind conditions (Hwang et al., 2010), making wind retrieval using a GMF impractical. The values of all re-tuned coefficients of the CSARMOD-GF are listed in Table 1.

Results

Figure 9 shows the calculations of NRCS using C-SARMOD, C-SARMOD2, and CSARMOD-GF for varying values of wind speed U_{10} and incidence angle θ for up-wind (φ = 0°) and cross-wind (φ = 90°) measurements. The CSARMOD-GF clearly performs differently from the C-SARMOD and C-SARMOD2. To further study the difference between the C-SARMOD2 and CSARMOD-GF, Figure 10 presents the bias of the simulated NRCS using the CSARMOD-GF and C-SARMOD2 in terms of the ECMWF wind speed for a 2 m/s bin, an incidence angle for a bin of about 3°, and an ECMWF wind direction for a 36° bin, in

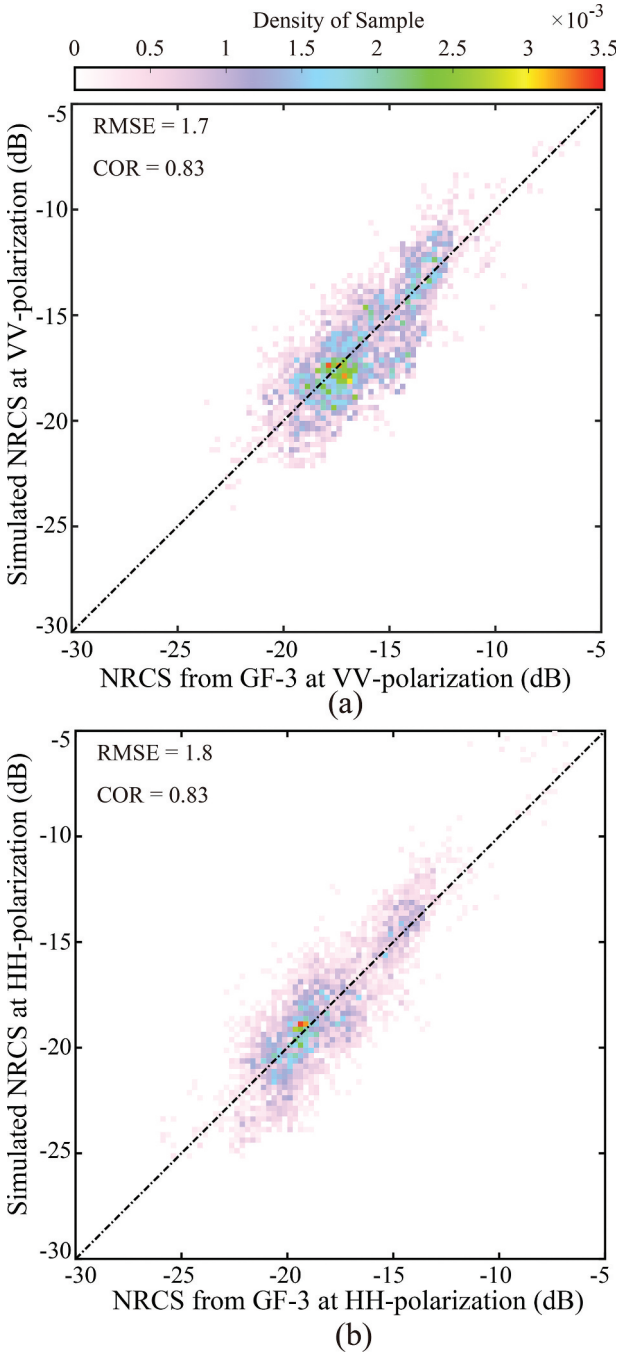

Figure 8. Relationship between NRCS calculated using CSARMOD-GF with NRCS measured at (a) VV-polarization, and (b) HH-polarization by the GF-3 SAR using the tuning dataset.

which the error bars represent the standard deviations of each bin. The variation of bias (with ±1 dB) increases at the wind speeds higher than 8 m/s (Figure 10a) and wind direction smaller 180° (Figure 10c), although the variation of bias decreases at incidence angles smaller than 34° (Figure 10b) and the variation of bias remains at 1 dB for increasing incidence angle. In other words, the CSARMOD-GF reduces the bias compared with C-SARMOD2 at incidence angles smaller than 34° and variation of bias has a stable deviation at incidence angles greater than 34°. We think the re-tuned coefficients in CSARMOD-GF improve the larger deviation using inaccurate calibration constants at low-to-moderate incidence. The newly released radiometric calibration information was used in this study; however, the calibration constants still necessitates the systematic improvement.

The test dataset includes approximately 700 GF-3 SAR images, collocated with ASCAT footprints, in which the CSARMOD-GF algorithm is applied. An example image obtained at 21:11 UTC 29 June 2017 in VV-polarization is depicted in Figure 11; wind speeds calculated from the proposed CSARMOD-GF algorithm (d) are contrasted with wind speeds

Table 1. Values of all coefficients in the CSARMOD-GF algorithm.

Polarization	Function	Coefficient	Value
VV	B_0	c_1	−4.76111036295841
HH			−4.10306388701714
VV		c_2	−6.76231077946305
HH			−3.35442907420696
VV		c_3	−6.00931934263315
HH			−1.37438621314482
VV		c_4	−3.01582440292399
HH			−1.39139207216787
VV		c_5	1.23293428211723
HH			1.59498337341745
VV		c_6	1.08049862434175
HH			1.37712467976484
VV		c_7	−1.10470253221469
HH			−1.05199843047151
VV		c_8	−1.03882761750926
HH			−0.947911013449889
VV		c_9	2.18304654814066
HH			2.06980324031277
VV		c_{10}	1.68180035932442
HH			−0.289877655131426
VV		c_{11}	3.44098741898235
HH			2.95301256301142
VV		c_{12}	−10.1735758314789
HH			−10.5760755641724
VV		c_{13}	−7.61034123719350
HH			−7.88879207585940
VV	B_1	c_{14}	−1.36990795795331
HH			0.396292223948731
VV		c_{15}	−2.76150089295021
HH			1.04453045932439
VV		c_{16}	−1.32438041496629
HH			0.619836688343114
VV		c_{17}	0.382868468051990
HH			−0.762400405957059
VV		c_{18}	0.823260239879638
HH			−1.53701390603189
VV		c_{19}	0.410279129480959
HH			−0.756701377652780
VV		c_{20}	−0.0299113765869897
HH			0.0672774287585950
VV		c_{21}	−0.0663469632439988
HH			0.132091109313581
VV		c_{22}	−0.0339243623147040
HH			0.0633225532378163
VV	B_2	c_{23}	0.800068480224308
HH			0.157613081677548
VV		c_{24}	0.431413827463545
HH			0.970592781760616
VV		c_{25}	−2.24750834762309
HH			−1.80328570865603
VV		c_{26}	−4.41986576373432
HH			−3.57676637986650
VV		c_{27}	−1.50586941357968
HH			−1.25444542401848
VV		c_{28}	16.0100785998030
HH			21.1125511772020
VV		c_{29}	−0.616348162438476
HH			−1.70969663034346
VV		c_{30}	−11.9376357912363
HH			−17.6856977086059
VV		c_{31}	15.4944706496630
HH			18.5642492542182
VV		c_{32}	12.9435336795741
HH			16.3869925561612

from other state-of-the-art methods: C-SARMOD (a), C-SARMOD2 (b), and CMOD7 (c). In Figure 12, comparisons of calculated wind speed are shown using a GF-3 SAR image obtained at HH-polarization three minutes later. Here, results using CSARMOD-GF (d) are compared to results using C-SARMOD (a), C-SARMOD2+ PR (b), and CMOD7+ PR (c). Note that the advanced PR model using the incidence angle and wind speed (B. Zhang et al., 2011) is priory employed for converting HH-polarization to VV-polarization NRCS when evaluating wind speeds by other GMFs, whereas no PR model is needed when applying CSARMOD-GF to HH-polarization SAR scenes. It is worth noting that

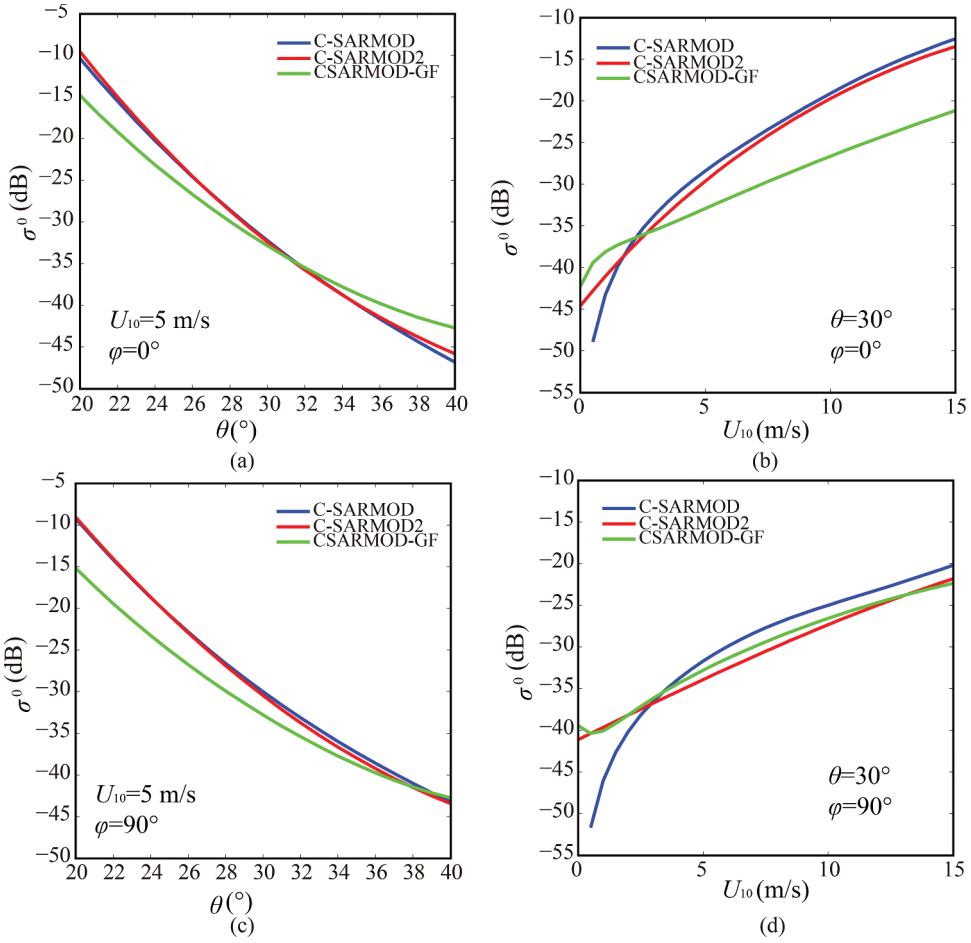

Figure 9. Computations of σ^0 using C-SARMOD, C-SARMOD2, and CSARMOD-GF for various values of wind speed U_{10} and incidence angle θ for up-wind (φ = 0°) and cross-wind (φ = 90°) measurements.

the GF-3 SAR data at (29.11 °N, 131.37 °E) is nearest to the ASCAT grid data at (29.13 °N, 131.38 °E), in which the ASCAT-measured wind is 6.6 m/s. In particular, there are slight discontinuities of SAR-derived wind maps using CMOD7 (Figures 11c and 12c), because CMOD7 is a look-up-table method which may cause a large gradient at a specific incidence angle.

Comparisons between ASCAT winds and winds derived from the entire dataset of VV-polarization GF-3 SAR images are shown in Figure 13, using wind speed bins of 1.6 m/s up to a maximum wind speed of 12.8 m/s, in which (a), (b), (c), and (d) show the relationship between ASCAT winds and winds calculated using C-SARMOD, C-SARMOD2, CMOD7, and CSARMOD-GF, respectively. An approximately 2.2 m/s RMSE is obtained using C-SARMOD, C-SARMOD2, and CMOD7, while smaller errors (RMSE = 1.77 m/s) are obtained using CSARMOD-GF. Validation results for HH-polarization GF-3 SAR images are shown in Figure 14, in which Figure 14a–c, and d show the relationship between ASCAT winds and winds calculated using C-SARMOD, C-SARMOD2+ PR (B. Zhang et al., 2011), CMOD7+ PR (B. Zhang et al., 2011), and CSARMOD-GF, respectively. The RMSE of wind speeds from HH-polarization images using CSARMOD-GF (1.85 m/s) is smaller than the RMSE using the other three methods (2.07–2.23 m/s). The comparisons of 231 matchups between HY-2B and SAR-derived winds at VV-polarization channel are presented in Figure 15, e.g., (a) using C-SARMOD (RMSE = 1.96 m/s), (b) using C-SARMOD2 (RMSE = 1.88 m/s), (c) using CMOD7 (RMSE = 2.40 m/s), and (d) using CSARMOD-GF (RMSE = 1.71 m/s). Similarly, Figures 16a–c, and d present the statistical results of SAR-derived winds at HH-polarization channel calculated using C-SARMOD, C-SARMOD2+ PR (B. Zhang et al., 2011), CMOD7+ PR (B. Zhang et al., 2011), and CSARMOD-GF, respectively, in which a 1.81 m/s RMSE is achieved using herein algorithm.

To further evaluate the applicability of the CSARMOD-GF algorithm, NDBC buoy data are used to verify wind speeds calculated using CSARMOD-GF and other retrieval algorithms. The statistical analysis of wind speeds calculated using the four algorithms is presented in Table 2 for VV-polarization and Table 3 for HH-

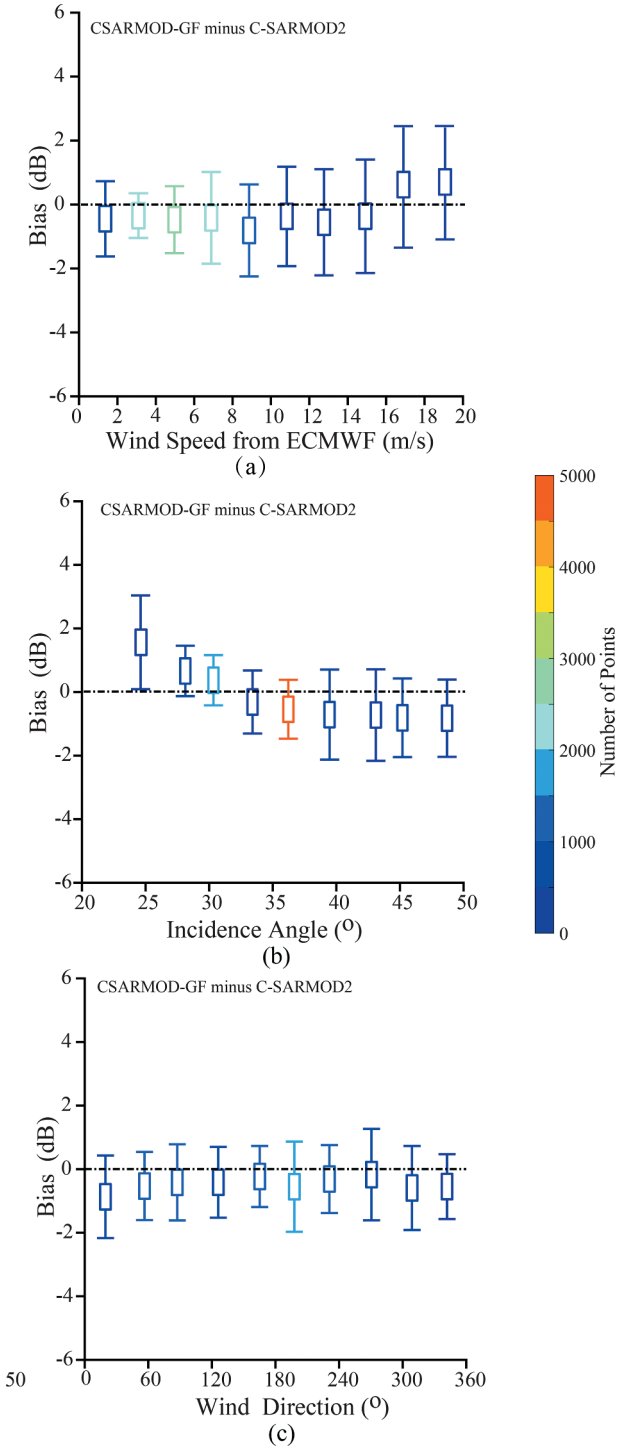

Figure 10. Bias of simulated NRCS using the CSARMOD-GF and C-SARMOD2 for various values of ECMWF wind speed, incidence angle, and ECMWF wind direction.

polarization. In Figures 17 and Figures 18, retrieval results from VV- and HH- polarization images, respectively, are compared with observations from NDBC buoys. The RMSE using CSARMOD-GF is for 1.71 m/s and 1.78 m/s for VV- and HH-polarization, respectively. These RMSE values are substantially smaller than the RMSE values obtained using other retrieval algorithms. However, the wind speeds calculated using CSARMOD-GF tend to be lower than buoy observations for observed wind speeds exceeding 3 m/s. We hypothesize that this is due to the ECMWF winds used to tune the CSARMOD-GF algorithm, which tend to be underestimated (Stopa & Cheung, 2014). Nevertheless, it is clear that the re-tuned CSARMOD-GF performs better than other state-of-the art methods when estimating wind speed using GF-3 imagery. The maximum wind speed for validation is also less then 14 m/s for ASCAT and 12 m/s for buoys. It is necessary to

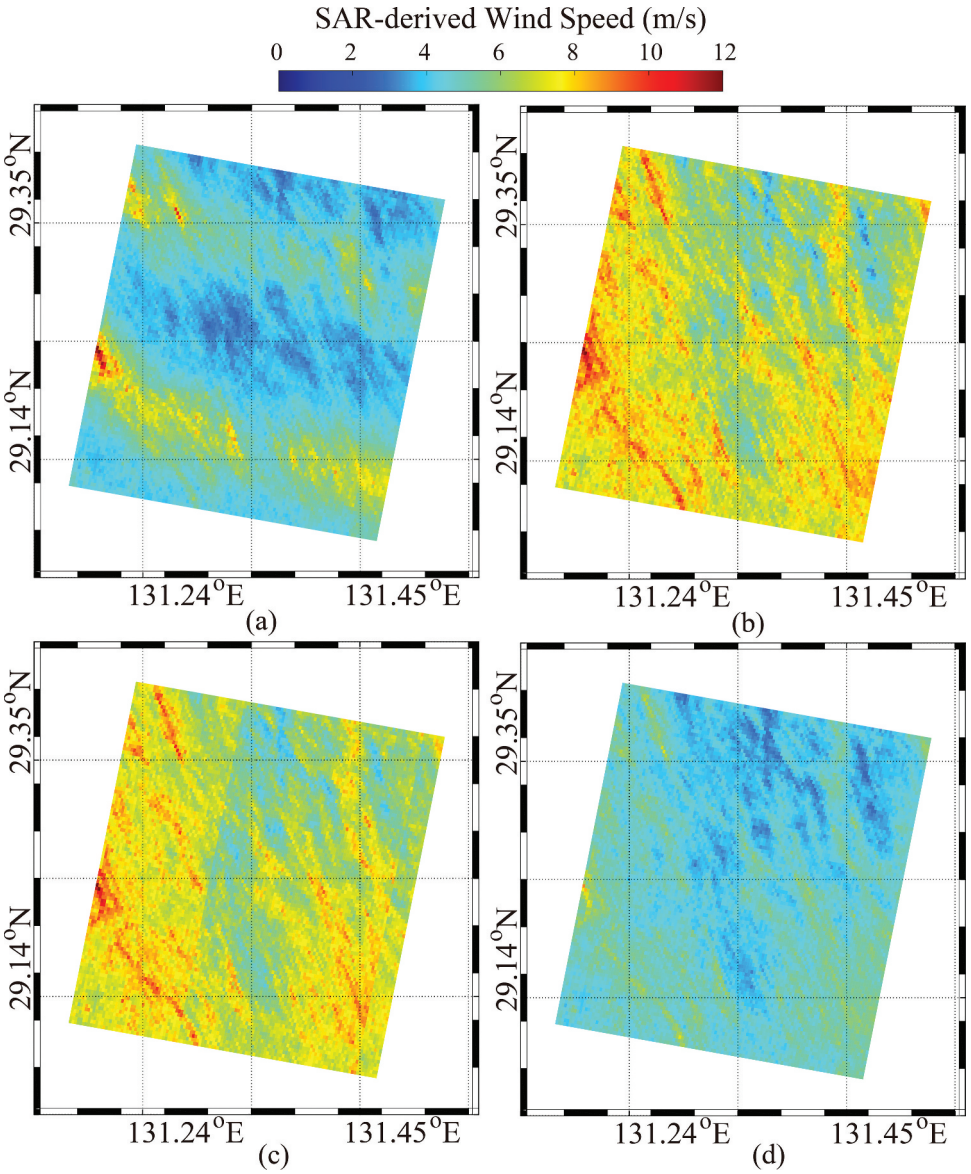

Figure 11. Wind speeds calculated from a VV-polarization GF-3 SAR image obtained at 21:14 UTC 29 June 2017. Wind speeds are obtained from: (a) C-SARMOD, (b) C-SARMOD2, (c) CMOD7, and (d) CSARMOD-GF.

figure out that the performance of the proposed algorithm at higher winds should be further examined.

Conclusions

Most wind retrieval algorithm GMFs that use C-band imagery are tuned using scatterometer-measured NRCS acquired in VV-polarization, which is assumed to behave somewhat differently than SAR imagery. The validation of SAR-derived winds from the GF-3 SAR images using the CMOD family, e.g., CMOD5 and CMOD5N, has been considered in recent studies (Ren et al., 2017), which showed that CMOD calculations are accurate to within approximately 2 m/s. As shown in Figure 5, it was discovered that the NRCS from GF-3 SAR exhibited a 2.8 dB deviation from the simulated NRCS using a well-known GMF CMOD5, a finding that prompted the development of wind retrieval for GF-3 SAR. Moreover, Lu et al. (2018) demonstrated improved accuracy using C-SARMOD2, which is directly tuned from SENTINEL-1A/1B SAR NRCS measurements and ancillary winds. The main goal of our work was to develop a specific GMF for wind retrieval from the GF-3 SAR images from both VV-polarization and HH-polarization channels.

The proposed CSARMOD-GF GMF was obtained using GF-3 SAR imagery in QPS/WV mode and collocated with the ECMWF winds, producing a wind speed correlation (R^2) of 0.83 and an RMSE of ~1.8 dB when the fitted results and the ECMWF winds were compared. We also further analyzed the NRCS bias (CSARMOD-GF simulations minus C-SARMOD2 simulations) in term of

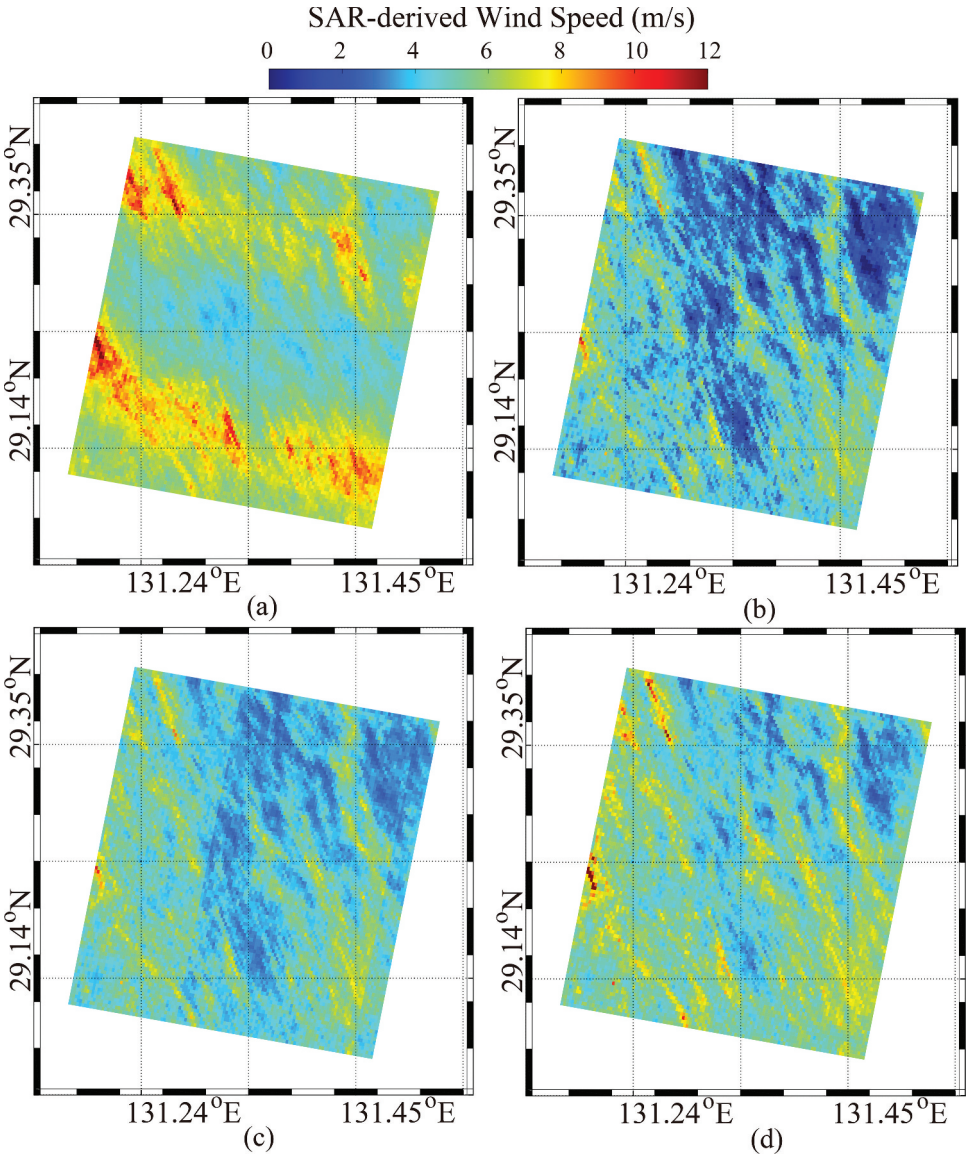

Figure 12. Wind speeds calculated from an HH-polarization GF-3 SAR image obtained at 21:14 UTC 29 June 2017. Wind speeds are obtained from: (a) C-SARMOD, (b) C-SARMOD2+ PR 2011, (c) CMOD7+ PR2011, and (d) CSARMOD-GF.

wind speed, incidence angle, and wind direction. The variation of bias was found to remain at ±1 dB with varying wind speed and wind direction. The variation of bias remained at 1 dB with increasing incidence angle, while decreasing at incidence angles <34°, indicating that the CSARMOD-GF differs significantly from the C-SARMOD2 at those conditions. This kind of behavior is likely caused by radiometric calibration at low-to-moderate incidence angles. The CSARMOD-GF was validated using a dataset that included GF-3 SAR images collocated with ASCAT winds, HY-2B winds and NOAA NDBC buoys. The validation results confirmed that the proposed CSARMOD-GF is able to operate on both VV- and HH-polarization channels without any external model for HH-polarization. The RMSE obtained using CSARMOD-GF was approximately 1.8 m/s for both VV- and HH-polarization, which is slightly smaller than from other state-of-the-art algorithms, generating a RMSE of approximately 2.0–2.4 m/s.

In the near future, this work will be extended to other image modes at more moderate winds (>10 m/s), such as Spotlight Mode, Standard Stripmap, Ultra Fine Stripmap, Global Observation, and Wide ScanSAR modes with the incidence angles ranged from 15° to 60°. Additionally, due to the inaccuracy of existing constants used for converting intensity of GF-3 image into NRCS resulting in the calibration uncertainty, we will work to improve the CSARMOD-GF using a larger tuning dataset obtained by revisiting the historical data.

Acknowledgments

The authors thank NSOAS, which provided the GF-3 SAR images through an authorized account via https://osdds.

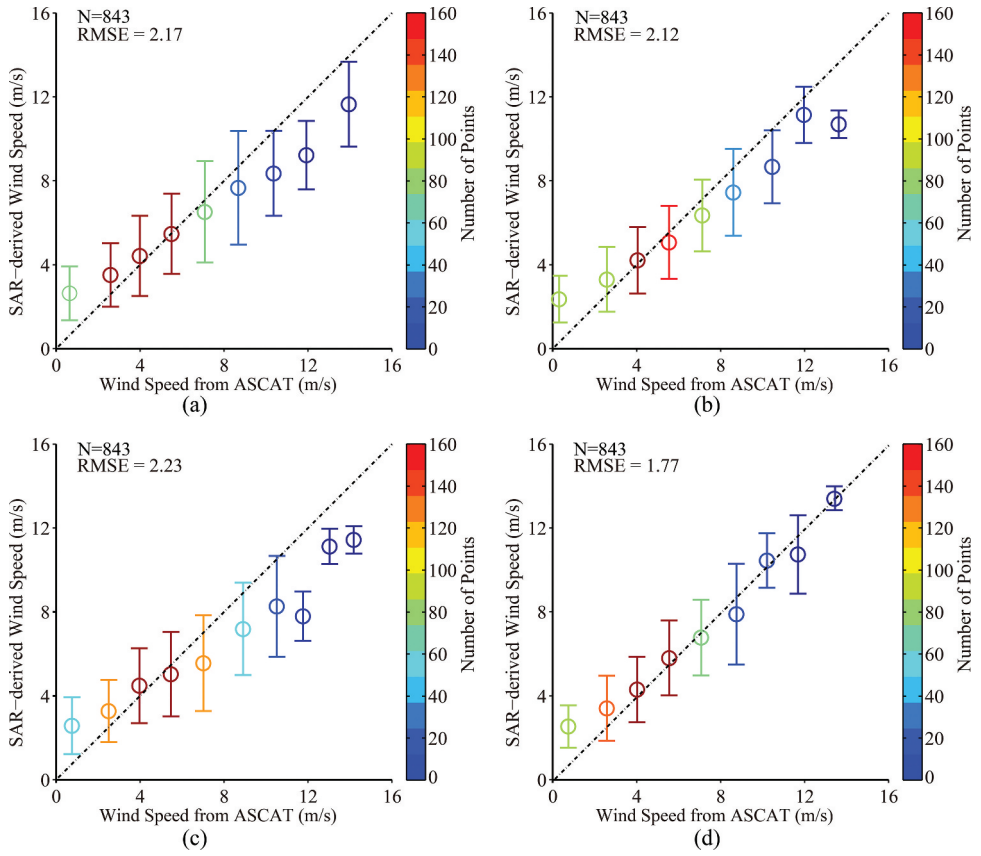

Figure 13. For the full test dataset of VV-polarization GF-3 SAR images, comparisons between ASCAT-derived wind speeds and wind speeds calculated using (a) C-SARMOD, (b) C-SARMOD2, (c) CMOD7, and (d) CSARMOD-GF. ASCAT wind speed bins of 1.6 m/s are used and the standard deviation of the calculated wind speed is shown for each bin.

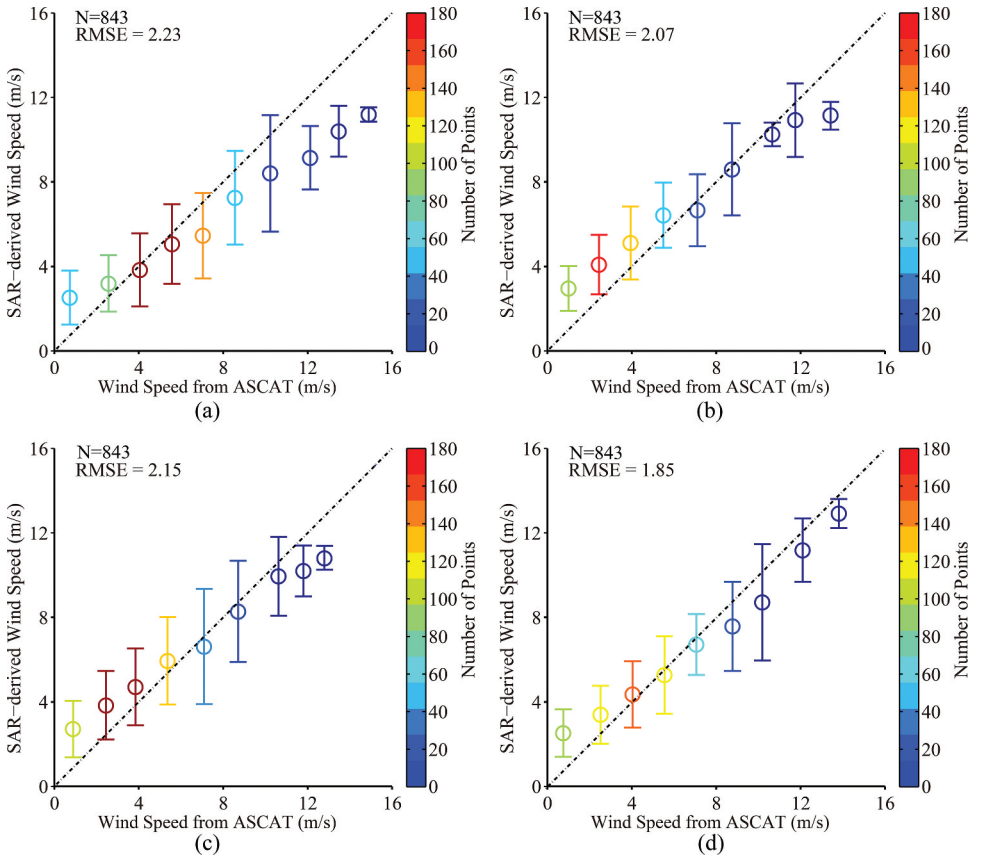

Figure 14. For the full test dataset of HH-polarization GF-3 SAR images, comparisons between ASCAT-derived wind speeds and wind speeds calculated using (a) C-SARMOD, (b) C-SARMOD2+ PR 2011, (c) CMOD7+ PR2011, and(d) CSARMOD-GF. ASCAT wind speed bins of 1.6 m/s are used and the standard deviation of the calculated wind speed is shown for each bin.

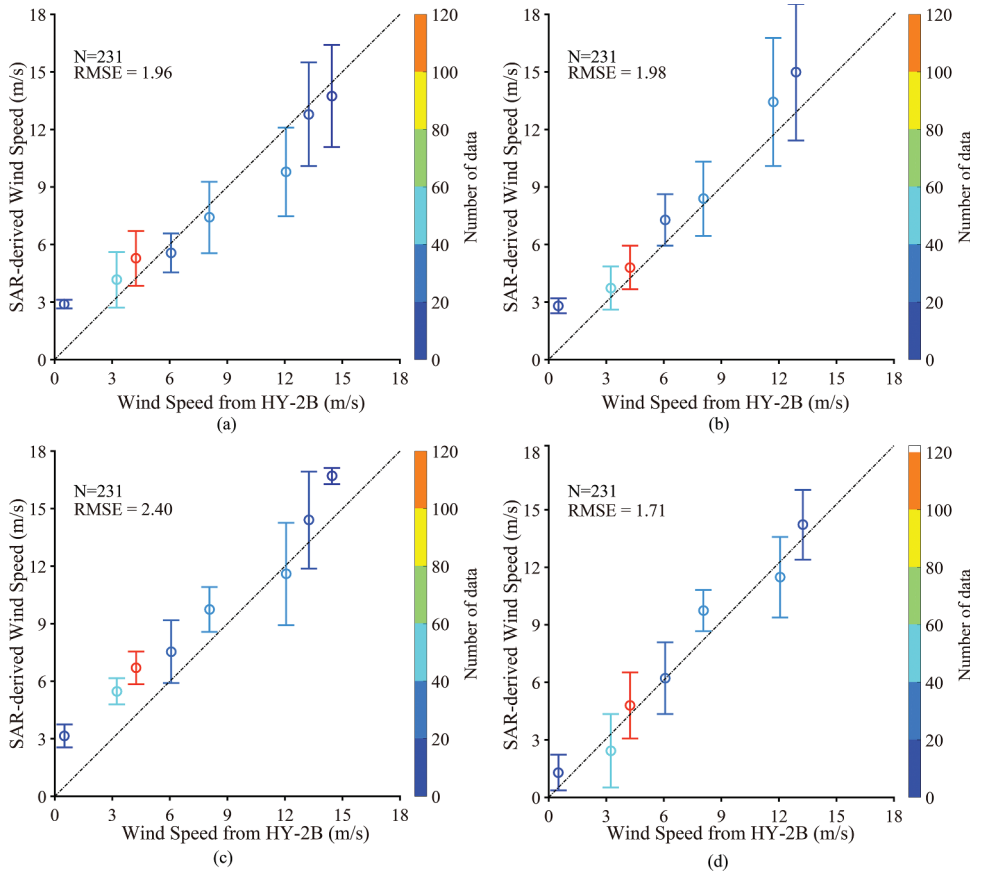

Figure 15. For the full test dataset of VV-polarization GF-3 SAR images, comparisons between wind speeds from HY-2B and wind speeds calculated using (a) C-SARMOD, (b) C-SARMOD2, (c) CMOD7, and (d) CSARMOD-GF. HY-2B wind speed bins of 1.8 m/s are used and the standard deviation of the calculated wind speed is shown for each bin.

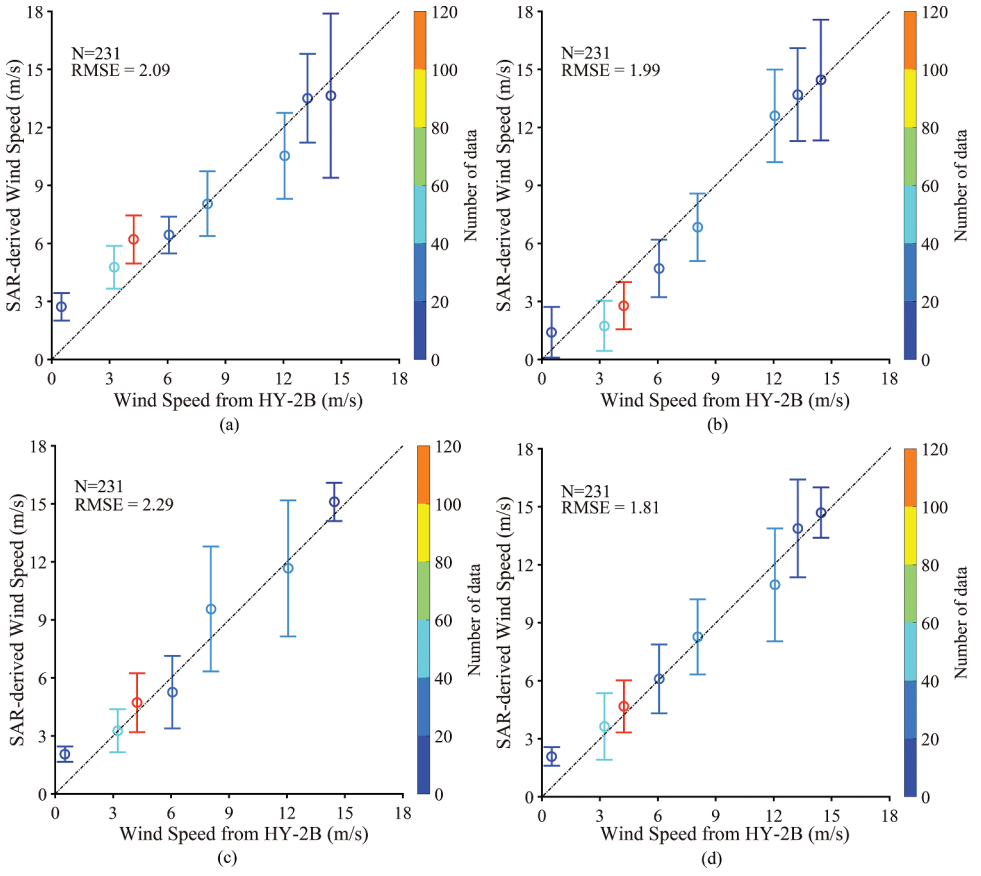

Figure 16. For the full test dataset of HH-polarization GF-3 SAR images, comparisons between wind speeds from HY-2B and wind speeds calculated using (a) C-SARMOD, (b) C-SARMOD2+ PR 2011, (c) CMOD7+ PR2011, and(d) CSARMOD-GF. HY-2B wind speed bins of 1.8 m/s are used and the standard deviation of the calculated wind speed is shown for each bin.

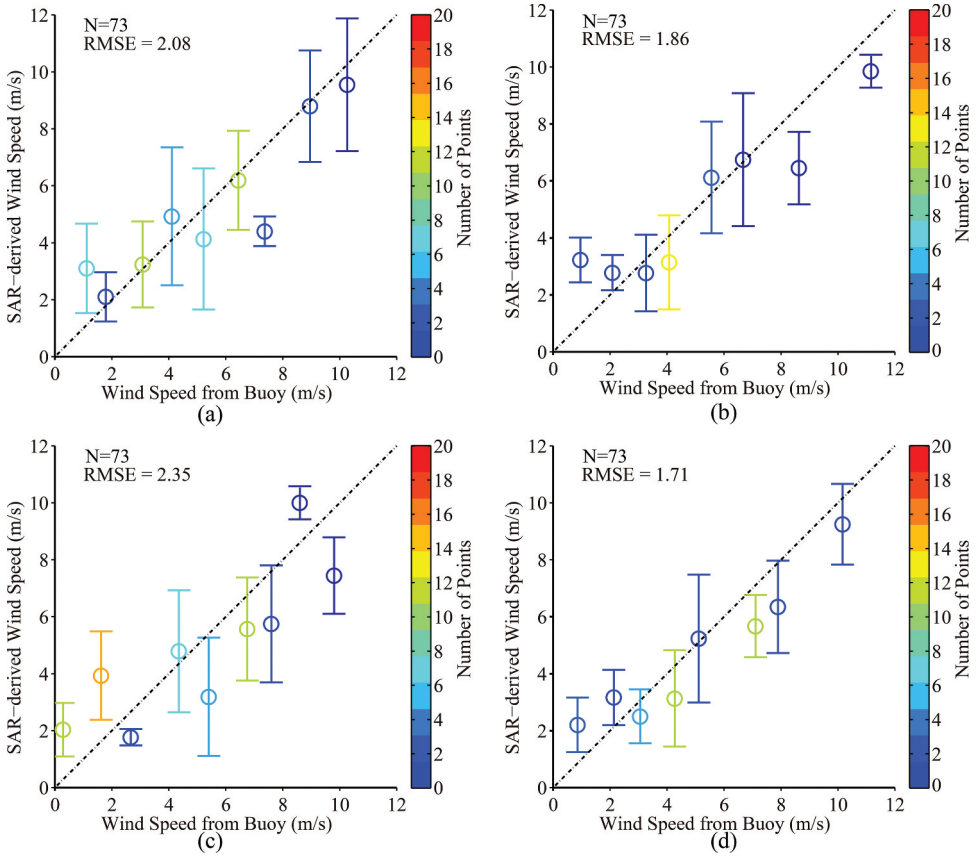

Figure 17. Comparison between wind speeds from NDBC buoy observations and wind speeds calculated from VV-polarization GF-3 imagery using (a) C-SARMOD, (b) C-SARMOD2, (c) CMOD7, and (d) CSARMOD-GF. NDBC wind speed bins of 1.2 m/s are used and the standard deviation of the calculated wind speed is shown for each bin.

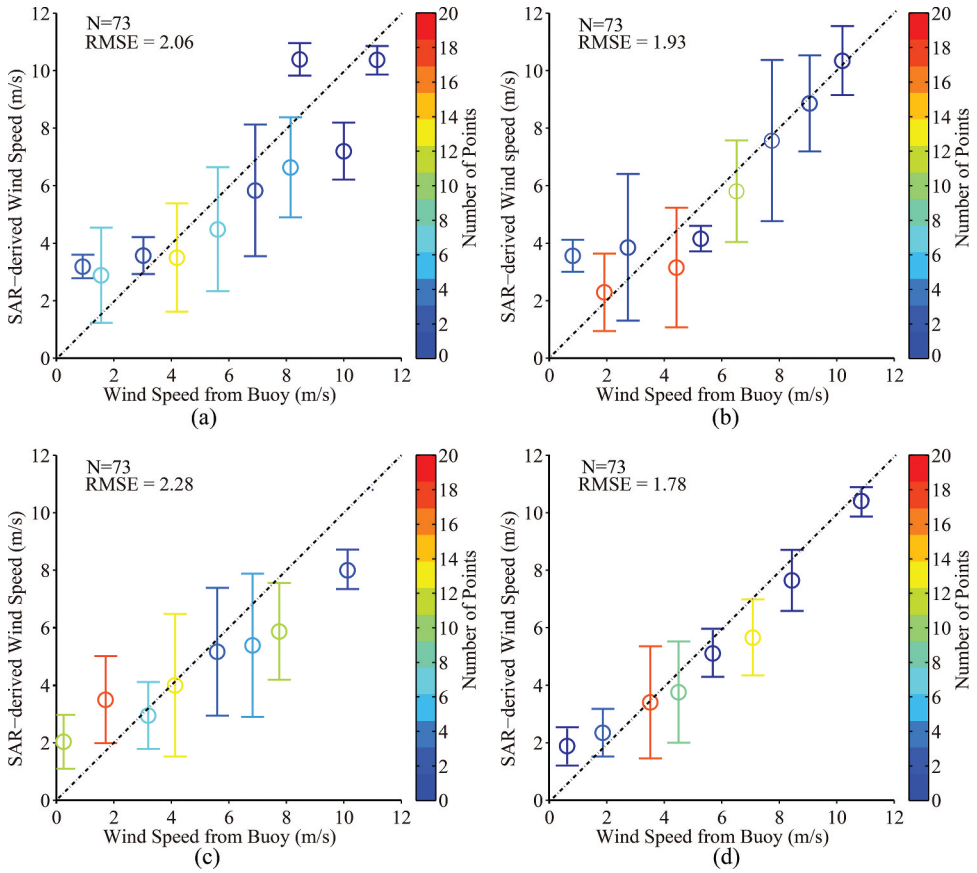

Figure 18. Comparison between wind speeds from NDBC buoy observations and wind speeds calculated from HH-polarization GF-3 imagery using (a) C-SARMOD, (b) C-SARMOD2+ PR model2011, (c) CMOD7+ PR model2011, (d) CSARMOD-GF. NDBC wind speed bins of 1.2 m/s are used and the standard deviation of the calculated wind speed is shown for each bin.

Table 2. Statistical analysis of SAR-derived wind speeds against buoy observations using four SAR algorithms for VV-polarized images.

Algorithm	Bias (m/s)	Root mean square error (m/s)	Standard deviation (m/s)	Scatter index (m/s)
CSARMOD	0.04	2.08	2.08	0.45
CSARMOD2	−0.21	1.86	1.85	0.46
CMOD7	0.31	2.35	2.33	0.57
CSARMOD-GF	−0.69	1.71	1.77	0.36

Table 3. Statistical analysis of SAR-derived wind speeds against buoy observations using four SAR algorithms for HH-polarized images.

Algorithm	Bias (m/s)	Root mean square error (m/s)	Standard deviation (m/s)	Scatter index (m/s)
CSARMOD	−0.20	2.06	2.05	0.45
CSARMOD2 + PR	−0.14	1.93	1.93	0.48
CMOD7 + PR	0.19	2.28	2.27	0.55
CSARMOD-GF	−0.49	1.78	1.71	0.41

nsoas.org.cn and the calibration document is available on the server ftp://osdds-ftp.nsoas.org.cn. ECMWF wind data were accessed via http://www.ecmwf.int. Measurements from NOAA NDBC buoys were downloaded via http://www.ndbc.noaa.gov and ASCAT winds were downloaded via http://archive.eumetsat.int using an authorized account.

Disclosure statement

No potential conflict of interest was reported by the author(s).

Funding

This research was partly supported by the National Natural Science Foundation of China under contract Nos. 41806005 and 42076238, and the China Postdoctoral Science Foundation under contract No. 2020M670245. This study was also partially funded under the framework of the Chinese Ministry of Science and Technology and ESA Dragon-4 program under contract No. 32235.

ORCID

Weizeng Shao http://orcid.org/0000-0003-3693-6217
Ferdinando Nunziata http://orcid.org/0000-0003-4567-0377

References

Alpers, W., & Brummer, B. (1994). Atmospheric boundary layer rolls observed by the synthetic aperture radar aboard the ERS-1 satellite. *Journal of Geophysical Research*, *99*(C6), 12613–12621. https://doi.org/10.1029/94jc00421

Chapron, B., Johnsen, H., & Garello, R. (2001). Wave and wind retrieval from SAR images of the ocean. *Annales Des Telecommunications*, *56*(11), 682–699. https://doi.org/10.1007/BF02995562

Choisnard, J., Power, D., Davidson, F., Stone, B., Howell, C., & Randell, C. (2007). Comparison of C-band SAR algorithms to derive surface wind vectors and initial findings in their use in marine search and rescue. *Canadian Journal of Remote Sensing*, *33*(1), 1–11. https://doi.org/10.5589/m07-002

Corcione, V., Grieco, G., Portabella, M., Nunziata, F., & Migliaccio, M. (2018). A Novel azimuth cutoff implementation to retrieve sea surface wind speed from SAR imagery. *IEEE Transaction on Geoscience and Remote Sensing*, *57*(6), 3331–3340. https://doi.org/10.1109/TGRS.2018.2883364

Fetterer, F., Gineris, D., & Wackerman, C. C. (1998). Validating a scatterometer wind algorithm for ERS-1 SAR. *IEEE Transactions on Geoscience and Remote Sensing*, *36*(2), 479–492. https://doi.org/10.1109/36.662731

Gerling, T. (1986). Structure of the surface wind field from the Seasat SAR. *Journal of Geophysical Research*, *91*(C2), 2308–2320. https://doi.org/10.1029/JC091iC02p02308

Grieco, G., Lin, W., Migliaccio, M., Nirchio, F., & Portabella, M. (2016). Dependency of the Sentinel-1 azimuth wavelength cut-off on significant wave height and wind speed. *International Journal of Remote Sensing*, *37*(21), 5086–5104. https://doi.org/10.1080/01431161.2016.1226525 9701–9708

Hasager, C. B., Mouche, A. A., Badger, M., BingoL, F., Karagali, I., Driesenaar, T., Stoffelen, A., Pena, A., & Longepe, N. (2015). Offshore wind climatology based on synergetic use of Envisat ASAR, ASCATand QuiksSACT. *Remote Sensing of Environment*, *156*(2015), 247–263. https://doi.org/10.1016/j.rse.2014.09.030

Hersbach, H. (2010). Comparison of C-Band scatterometer CMOD5.N equivalent neutral winds with ECMWF. *Journal of Atmospheric and Oceanic Technology*, *27*(4), 721–736. https://doi.org/10.1175/2009JTECHO698.1

Hersbach, H., Stoffelen, A., & Haan, S. D. (2007). An improved C-band scatterometer ocean geophysical model function: CMOD5. *Journal of Geophysical Research*, *112*(C3), C03006. https://doi.org/10.1029/2006JC003743

Hwang, P., Zhang, B., Toporkov, J., & Perrie, W. (2010). Comparison of composite Bragg theory and quad-polarization radar backscatter from Radarsat-2: With applications to wave breaking and high wind retrieval. *Journal of Geophysical Research*, *115*(C11), 246–255. https://doi.org/10.1029/2009JC005995

Koch, W., & Feser, F. (2006). Relationship between SAR-derived wind vectors and wind at 10-m height represented by a mesoscale model. *Monthly Weather Review*, *134*(5), 1505–1517. https://doi.org/10.1175/mwr3134.1

Komarov, S., Komarov, A., & Zabeline, V. (2011). Marine wind speed retrieval from RADARSAT-2 dual-polarization imagery. *Canadian Journal of Remote Sensing*, *37*(No. 5), 520–528. https://doi.org/10.5589/m11-063

Komarov, S., Zabeline, V., & Barber, D. (2013). Ocean surface wind speed retrieval from C-band SAR images without wind direction input. *IEEE Transactions on Geoscience and Remote Sensing*, *52*(No. 2), 980–990. https://doi.org/10.5589/m11-063

La, T. V., Khenchaf, A., Comblet, F., & Nahum, C. (2018). Assessment of wind speed estimation from C-band

Sentinel-1 images using empirical and electromagnetic models. *IEEE Transactions on Geoscience and Remote Sensing*, *56*(No.7), 4075–4087. https://doi.org/10.1109/TGRS.2018.2822876

Li, X. M., Lehner, S., & Bruns, T. (2011). Ocean wave integral parameter measurements using Envisat ASAR wave mode data. *IEEE Transactions on Geosciences and Remote Sensing*, *49*(No. 1), 155–174. https://doi.org/10.1109/TGRS.2010.2052364

Li, X. M., Zhang, T., Huang, B., & Jia, T. (2018). Capabilities of Chinese Gaofen-3 synthetic aperture radar in selected topics for coastal and ocean observations. *Remote Sensing*, *10*(11), 155–174. https://doi.org/10.3390/rs10121929

Lu, Y., Zhang, B., Perrie, W., Li, X. F., & Wang, H. (2018). A C-band geophysical model function for determining coastal wind speed using synthetic aperture radar. *IEEE Journal of Selected Topics in Applied Earth Observations and Remote Sensing*, *11*(No.7), 2417–2428. https://doi.org/10.1109/JSTARS.2018.2836661

Masuko, H., Okamoto, K., Shimada, M., & Niwa, S. (1986). Measurement of Microwave backscattering signatures of the ocean surface using X band and Ka band airborne scatterometers. *Journal of Geophysical Research*, *91*(No. C11), 13065–13083. https://doi.org/10.1029/JC091iC11p13065

Monaldo, F. M., Jackson, C., Li, X. F., & Pichel, W. (2016). Preliminary evaluation of Sentinel-1A wind speed retrievals. *IEEE Journal of Selected Topics in Applied Earth Observations and Remote Sensing*, *9*(No. 6), 2638–2642. https://doi.org/10.1109/JSTARS.2015.2504324

Quilfen, Y., Chapron, B., Elfouhaily, T., Katsaros, K., & Tournadre, J. (1998). Observation of tropical cyclones by high-resolution scatterometry. *Journal of Geophysical Research Oceans*, *103*(C4), 7767–7786. https://doi.org/10.1029/97JC01911

Remmers, T., Cawkwell, F., Desmond, C., Murphy, J., & Politi, E. (2019). The Potential of Advanced Scatterometer (ASCAT) 12.5 km Coastal Observations for Offshore Wind Farm Site Selection in Irish Waters. *Energies*, *12*(No.2), 206–221. https://doi.org/10.3390/en12020206

Ren, L., Yang, J. S., Mouche, A. A., Wang, H., Wang, J., & Zheng, G. (2017). Preliminary analysis of Chinese GF-3 SAR quad-polarization measurements to extract winds in each polarization. *Remote Sensing*, *9*(No. 12), 1215. https://doi.org/10.3390/rs9121215

Shao, W. Z., Li, X. M., Lehner, S., & Guan, C. L. (2014). Development of polarization ratio model for sea surface wind field retrieval from TerraSAR-X HH polarization data. *International Journal of Remote Sensing*, *35*(11–12), 4046–4063. https://doi.org/10.1080/01431161.2014.916059

Shao, W. Z., Sheng, Y. X., & Sun, J. (2017). Preliminary assessment of wind and wave retrieval from Chinese Gaofen-3 SAR imagery. *Sensors*, *17*(No. 8), 1705. https://doi.org/10.3390/s17081705

Shao, W. Z., Zhu, S., Sun, J., Yuan, X. Z., Sheng, Y. X., Zhang, Q. J., & Ji, Q. Y. (2019a). Evaluation of wind retrieval from co-polarization Gaofen-3 SAR imagery around China Seas. *Journal of Ocean University of China*, *18*(No. 1), 80–92. https://doi.org/10.1007/s11802-019-3779-8

Shao, W. Z., Zhu, S., Zhang, X. P., Gou, S. P., Jiao, C. Z., Yuan, X. Z., & Zhao, L. B. (2019b). Intelligent wind retrieval from Chinese Gaofen-3 SAR imagery in quad-polarization. *Journal of Atmospheric and Oceanic Technology*, *36*(No. 11), 2121–2137. https://doi.org/10.1175/JTECH-D-19-0048.1

Sheng, Y. X., Shao, W. Z., Zhu, S., Sun, J., Yuan, X. Z., Li, S., Shi, J., & Zuo, J. (2018). Validation of significant wave height retrieval from co-polarization Chinese Gaofen-3 SAR imagery using an improved algorithm. *Acta Oceanologica Sinica*, *37*(6), 1–10. https://doi.org/10.1007/s13131-018-1217-1

Stoffelen, A., & Anderson, D. (1997). Scatterometer data interpretation: Estimation and validation of the transfer function CMOD4. *Journal of Geophysical Research Oceans*, *102*(No. C3), 5767–5780. https://doi.org/10.1029/96JC02860

Stoffelen, A., Verspeek, J. A., Vogelzang, J., & Verhoef, A. (2017). The CMOD7 geophysical model function for ASCAT and ERS wind retrievals. *IEEE Journal of Selected Topics in Applied Earth Observations and Remote Sensing*, *10*(No. 5), 2123–2134. https://doi.org/10.1109/JSTARS.2017.2681806

Stopa, J. E., & Cheung, K. F. (2014). Intercomparison of wind and wave data from the ECMWF Reanalysis Interim and the NCEP Climate Forecast System Reanalysis. *Ocean Modelling*, *75*(No. 2014), 65–83. https://doi.org/10.1016/j.ocemod.2013.12.006

Vachon, P. W., & Dobson, F. W. (2000). Wind retrieval from RADARSAT SAR images: Selection of a suitable C-band HH polarization wind retrieval model. *Canadian Journal of Remote Sensing*, *26*(No. 4), 306–313. https://doi.org/10.1080/07038992.2000.10874781

Vogelzang, J., Stoffelen, A., Verhoef, A., & Figa-Saldana, J. (2011). On the quality of high-resolution scatterometer winds. *Journal of Geophysical Research*, *116*(No. C10), C10033. https://doi.org/10.1029/2010JC006640

Wang, L., Han, B., Yuan, X. Z., Lei, B., Ding, C. B., Yao, Y. L., & Chen, Q. (2018). A preliminary analysis of wind retrieval, based on GF-3 wave mode data. *Sensors*, *18*(5), 1604. https://doi.org/10.3390/s18051604

Yang, X. F., Li, X. F., Pichel, W., & Li, Z. W. (2011b). Comparison of ocean surface winds from ENVISAT ASAR, Metop ASCAT scatterometer, buoy Measurements, and NOGAPS model. *IEEE Transactions on Geoscience and Remote Sensing*, *49*(No. 12), 4743–4750. https://doi.org/10.1109/tgrs.2011.2159802

Yang, X. F., Li, X. F., Zheng, Q. A., Gu, X., Pichel, W., & Li, Z. W. (2011a). Comparison of ocean-surface winds retrieved from QuikSCAT scatterometer and Radarsat-1 SAR in offshore waters of the U.S. west coast. *IEEE Geoscience and Remote Sensing Letters*, *8*(No. 1), 163–167. https://doi.org/10.1109/lgrs.2010.2053345

Zhang, B., Perrie, W., & He, Y. J. (2011). Wind speed retrieval from RADARSAT-2 quad-polarization images using a new polarization ratio model. *Journal of Geophysical Research*, *116*(No. C8), 1318–1323. https://doi.org/10.1029/2010JC006522

Zhang, T., Li, X. M., Feng, Q., Ren, Y., & Shi, Y. (2019). Retrieval of sea surface wind speeds from Gaofen-3 full polarimetric data. *Remote Sensing*, *11*(No. 7), 813. https://doi.org/10.3390/rs11070813

Zhao, Y., Li, X. M., & Sha, J. (2016). Sea surface wind streaks in spaceborne synthetic aperture radar imagery. *Journal of Geophysical Research*, *121*(No. 9), 6731–6741. https://doi.org/10.1002/2016JC012040

Zhou, L., Zheng, G., Li, X. F., Yang, J. S., Ren, L., Chen, P., Zhang, H., & Lou, X. (2017). An improved local gradient method for sea surface wind direction retrieval from SAR imagery. *Remote Sensing*, *9*(No. 7), 671. https://doi.org/10.3390/rs9070671

Zhu, S., Shao, W. Z., Armando, M., Shi, J., Sun, J., Yuan, X. Z., Hu, J. C., Yang, D. K., & Zuo, J. C. (2018). Evaluation of Chinese quad-polarization Gaofen-3 SAR wave mode data for significant wave height retrieval. *Canadian Journal of Remote Sensing*, *44*(No. 6), 588–600. https://doi.org/10.1080/07038992.2019.1573136